International Journal of
Automotive Manufacturing and Materials（IJAMM）

Scilight

Article

Effect of Inlet Diameter on the Temperature of Hydrogen Fuel Tanks for Automotive Applications

Matthieu Guttinger, and Jean-Baptiste R. G. Souppez *

Department of Mechanical, Biomedical and Design Engineering, School of Engineering and Technology, College of Engineering and Physical Sciences, Aston University, Birmingham B4 7ET, UK

* Correspondence: j.souppez@aston.ac.uk

Received: 14 June 2024; Revised: 26 August 2024; Accepted: 29 August 2024; Published: 4 September 2024

Abstract: Contemporary concerns for sustainability have prompted a move away from fossil fuels, with hydrogen being a promising alternative. In the automotive field, Type III hydrogen tanks allow for high pressures to be achieved while being lightweight and small. Their size makes them particularly sensitive to small changes in inlet diameter, which is crucial to ensuring the strict regulatory requirements for internal tank temperatures are met. However, there remains a lack of understanding of the effect of inlet diameter on the internal temperature of Type III hydrogen tanks, needed for the next generation of gaseous hydrogen regulations for land vehicles. Consequently, this paper employs computational fluid dynamics to quantify the effect of the inlet diameter for values ranging from 5 mm to 15 mm on the temperature of Type III hydrogen tanks, of internal diameter 354 mm, to comply with current automotive regulations. Here, we show that (i) an increase in inlet diameter results in a monotonic increase in internal tank temperature; (ii) a linear interpolation between the mass flow rates investigated in this study may be employed to estimate the temperature at a given inlet diameter; and (iii) pre-cooling has an impactful effect and enables control of the internal tank temperature to avoid exceeding regulatory maximum temperature, irrelevant of inlet diameter. Lastly, we provide recommendations on analysing thermal results to ensure the safety of hydrogen tanks by design, with a particular emphasis on temperature hotspots forming upstream of the inlet. These results provide novel insights into the effect of inlet diameter and pre-cooling on the temperature of hydrogen tanks for automotive applications and inform their design to meet relevant regulations inherent to their filling. Moreover, these findings are anticipated to contribute to future regulatory development and the wider adoption of hydrogen as a sustainable fuel.

Keywords: hydrogen storage; type III hydrogen tank; pre-cooling; computational fluid dynamics (CFD); automotive vehicles

1. Introduction

Alternative fuels for both on and off-highway industries have received continuous interest in their development as governing bodies worldwide entertain solutions for reducing vehicle exhaust emissions to steer away from fossil fuel usage [1,2]. Alongside hybrid and electric solutions, hydrogen fuel technologies are increasingly viable, particularly in the automotive sector, as evidenced by the growing commercial transportation applications such as buses and lorries [3–5].

At ambient pressure, hydrogen gas has a volumetric energy density of 3.5 kWh/m^3, in contrast to 9000 kWh/m^3 for gasoline [6]. Consequently, hydrogen gas is compressed to a maximum pressure of 70 MPa, as dictated by the Society of Automotive Engineers (SAE) J2601 standard [7], thereby resulting in a volumetric energy density of 1500 kWh/m^3 [6]. Three main solutions have been proposed to alleviate the comparatively lower volumetric energy density of hydrogen, namely high-pressure hydrogen tanks, liquid hydrogen tanks and materials that absorb and store hydrogen [8]. However, high-pressure tanks appear as the

most viable solution at present and thus are found on currently operating vehicles [3–5]. In contrast, liquid hydrogen needing to be stored at 25 K (circa −248 °C) requires a significant amount of energy, which acts as a cost and infrastructure deterrent, while storing hydrogen in a solid state thanks to absorbent materials still faces critical challenges [9]. High-pressure hydrogen tanks are, therefore, seen as the most relevant present solution for automotive applications [10].

The design and manufacturing of compressed hydrogen gas tanks are governed by the International Standard of Organisation (ISO) 19881:2018 [11], while the SAE J2601 [7] governs its operational usage. Both standards are compatible with each other and make references to their counterpart. This will remain true for the revised ISO 19881, to be published in 2025. Both taxonomies categorise hydrogen tanks into four types (Type I – IV), each with increasing complexity of material structure representing the transition of traditional aluminium/steel tanks to carbon fibre/polymer tanks. Owing to the automotive focus of this paper, its scope is restricted to Type III hydrogen tanks, defined as constructed of composite with a metallic liner. The operation is further divided into two categories of nominal working pressures (NWP): 35 MPa and 70 MPa.

During filling, the inlet pressure is ramped from 0 MPa (empty) or 2 MPa (almost empty) up to the NWP of either 35 MPa or 70 MPa, as relevant. The pressure increase rate needs to adhere to the J2601 standard, with a linear increase employed in both experimental and numerical studies [12–17]. As the high-pressure hydrogen is jettisoned through the inlet, it compresses the gas directly opposite to the inlet against the tank wall. Consequently, Charles's law is observed as the temperature increases as a result of the increase in pressure. This leads to heat transfer into the liner and subsequent wall materials, as experimentally confirmed by [18].

With the short refuelling time of a maximum of 180 s required by the J2601 standard for automotive applications, the increase in pressure over a short duration poses a challenge for temperature control in ensuring that the tank does not exceed the regulatory 358 K limit (~85 °C). As a result, hydrogen pre-cooling is required [13], as repeated thermal stress can accelerate fatigue of the composite materials for certain tank types [19, 20], including the Type III tanks under consideration. Pre-cooling is defined as the act of intentionally reducing the temperature of the hydrogen gas before the inlet and is an effective means to reduce the overall temperature of the tank [21,22], albeit at the cost of added energy consumption [23]. Such alteration of the tank operation influences the temperature [24,25], as does the geometry. However, the latter has been comparatively less investigated, particularly for small Type III tanks, where the inlet-diameter-to-tank-diameter ratio becomes significant. Indeed, while some inlet diameters have been considered for automotive [12] and marine [15] applications, the effect of a large range of diameters on the internal temperature of hydrogen tanks remains to be characterised.

Consequently, this paper aims to provide novel insights into the effect of inlet diameter on the temperature of Type III hydrogen tanks for automotive applications by employing computational fluid dynamics (CFD). Specifically, because the smaller Type III tanks for automotive applications feature a higher inlet-diameter-to-tank-diameter ratio, and temperature is crucial for safety, we aim to quantify how larger diameters affect the temperature. This work will enable the enhancement of the regulatory framework for land vehicles employing gaseous hydrogen fuel containers, such as ISO 19881 [11].

The remainder of this paper is structured as follows. First, Section 2 details the methodology employed, including the governing equations, geometry and materials properties, numerical setup, and verification and validation undertaken. Then, Section 3 presents results for the effect of the inlet diameter on the temperature, with and without pre-cooling, for different mass flow rates. Finally, Section 4 summarises the main findings of this study and their broader impact.

2. Methodology

2.1. Governing Equations

Numerical simulations are undertaken using Ansys Fluent R23, where the Navier-Stokes system of equation applies [26], namely:

(1) conservation of mass:

$$\frac{\partial \rho}{\partial t} + \nabla \cdot \left(\rho \vec{v} \right) = 0, \tag{1}$$

(2) conservation of momentum:

$$\frac{\partial}{\partial t}\left(\rho \vec{v} \right) + \nabla \cdot \left(\rho \vec{v} \vec{v} \right) = -\nabla p + \nabla \cdot \left(\underline{\tau} \right) + \rho g, \tag{2}$$

(3) conservation of energy:

$$\frac{\partial}{\partial t}\left(\rho E \right) + \nabla \cdot \left(\vec{v}\left(\rho E + p \right) \right) = \nabla \cdot \left\{ k_{\text{geff}} \nabla T + \left[\underline{\tau} \cdot \vec{v} \right] \right\}, \tag{3}$$

where t is the time, ρ is the density, $\vec{v}$ is the Favre average of velocity, p is the static pressure, $\underline{\tau} = \mu\left[\nabla \vec{v} - \frac{2}{3} \times \nabla \cdot \vec{v} \right]$ is the stress tensor, E is the energy, μ is the dynamic viscosity, I is the unit tensor, and k_{geff} is the effective thermal conductivity.

The rate of energy increase is given by

$$\frac{\partial \left(\rho i \right)}{\partial t} + \operatorname{div}\left(\rho i u \right) = -p \operatorname{div} u + \left(k \operatorname{grad} T \right) + \Phi + S_i, \tag{4}$$

where i is the turbulence intensity factor, k is the turbulent kinetic energy, T is the temperature, Φ is the dissipation function, and S_i is source term relating to turbulence intensity.

Moreover, the present simulations are conducted using the $k-\varepsilon$ turbulence model [27]. This has proven successful in modelling the rapid charging of hydrogen in storage tanks, was validated against published results (See Section 2.3), and has commonly been employed for the numerical modelling of rapid charging hydrogen tanks by [28–32], and given as

$$\frac{\partial \left(\rho k \right)}{\partial \mathrm{t}} + \frac{\partial \left(\rho k u \right)}{\partial \mathrm{x_i}} = \frac{\partial}{\partial x_j}\left[\left(\mu + \frac{\mu_t}{\sigma_k} \right) \frac{\partial k}{\partial x_j} \right] + G_k + G_b - \rho\varepsilon - Y_M + S_k, \tag{5}$$

$$\frac{\partial \left(\rho \varepsilon \right)}{\partial t} + \frac{\partial \left(\rho \varepsilon u \right)}{\partial x_i} = \frac{\partial}{\partial x_j}\left[\left(\mu + \frac{\mu_t}{\sigma_\varepsilon} \right) \frac{\sigma\varepsilon}{\partial x_j} \right] + C_{1\varepsilon} \frac{\varepsilon}{k}\left(G_k + C_{3\varepsilon} G_b \right) - C_{2\varepsilon} \rho \frac{\varepsilon^2}{k} + S_\varepsilon, \tag{6}$$

and

$$\mu_t = \rho C_\mu \frac{k^2}{\varepsilon}, \tag{7}$$

where μ_t is the eddy viscosity, G_k is the turbulent kinetic energy generation due to the mean velocity gradients, G_b is the turbulent kinetic energy generation due to buoyancy, Y_M is the contribution of the fluctuating dilatation in compressible turbulence to the overall dissipation rate and σ, σ_ε, $C_{1\varepsilon}$, $C_{2\varepsilon}$, $C_{3\varepsilon}$, C_μ are constants.

Finally, the heat flux q_1'' for conduction and q_2'' for convection is given as

$$q_1'' = -\lambda \frac{\mathrm{d}T}{\mathrm{d}x}, \tag{8}$$

and

$$q_2'' = hA\left(T_w - T_\infty \right), \tag{9}$$

where λ is the thermal conductivity, h is the convective heat transfer coefficient taken as 10 W/m^2 K [31], A is the area of the contact region, T_w is the wall temperature, and T_∞ is the surrounding temperature.

Such a numerical approach is justified by the significant advances in the understanding of hydrogen tanks achieved thanks to CFD [12–15,17–20,25,27–30,32,33].

2.2. Numerical Setup

The sphero-cylindrical geometry adopted is that investigated by [25, 33], omitting the end cylindrical bosses for the numerical simulations, as depicted in Figure 1. The inner length of the tank is $L = 849$ mm, and

the inner diameter is $D = 354$ mm, yielding an internal volume $V = 74.3$ L. The inlet tube extends by a length $l = 0.67$ mm inside of the tank ($l/L = 0.00137$), and has an inner diameter ranging from $d = 5$ mm ($d/D = 0.0141$) to $d = 15$ mm ($d/D = 0.0424$), investigated in Section 3.

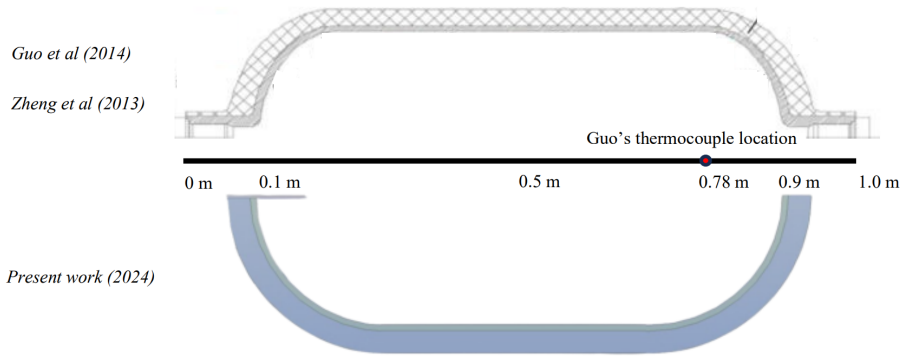

Figure 1. Comparison between the benchmark hydrogen tank geometry of [25,33] (top) and that employed in this study (bottom).

The tank is a 70 MPa NWP Type III with an inner 10~mm aluminium liner ($\rho = 2700$ kg/m^3, $c = 902$ J/kg K, and $\lambda = 238$ W/m K) surrounded by 28 mm of carbon fibre-reinforced polymer (CFRP) ($\rho = 1570$ kg/m^3, $c = 840$ J/kg K, and $\lambda = 0.612$ W/m K). A 1 mm thick layer of glass fibre-reinforced polymer (GRP) (where $\rho = 2050$ kg/m^3, $c = 878$ J/kg K, and $\lambda = 0.133$ W/m K) further surrounds the CFRP, as is found in road vehicles. The GRP is intended to prevent scratches and abrasions. Therefore, we anticipate this to have no bearing on the results as the internal fluid region is significantly larger than the GRP region. The tank is surrounded by ambient air at $T = 293$ K.

The tank is filled with a linear increase in pressure from $P = 0$ MPa at $t = 0$ s to $P = 70$ MPa at $t = 180$ s, i. e., the regulatory maximum allowed [7], with the inlet at $T = 288$ K at $t = 0$ s. The hydrogen properties employed in this study are based on the Redlich-Kwong model [34], as adopted by [12,35].

2.3. Verification and Validation

A structured 2D mesh was applied throughout the computational domain, as shown in Figure 2, with an average element size of 4 mm and a minimum edge size of 1 mm. A grid independence study was undertaken to demonstrate that convergence was reached. This was conducted in accordance with the Celik et al. error estimation [36] and Richardson discretization [37], as recommended by [38].

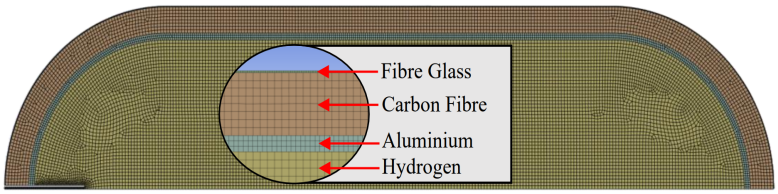

Figure 2. Structured mesh employed for this study, with details of the tank's outer structure comprised of 10 mm aluminium, 27 mm carbon fibre-reinforced polymer (CFRP) and 1 mm glass fibre-reinforced polymer (GRP).

First, the grid size h from the fine (h_1), medium (h_2) and coarse (h_3) mesh is ascertained as

$$h = \left[\frac{1}{N} \sum_{i=1}^{N} (\Delta A_i) \right]^{1/2}, \tag{10}$$

where N is the number of elements and ΔA_i is the area of the i^{th} cell.

Then, the refinement factors $r_{21} = h_2/h_1$ and $r_{32} = h_3/h_2$, both to be greater than 1.3 [38] are computed, followed by the apparent order p_a given as

$$p_a = \frac{1}{\ln\left(r_{21}\right)}\left|\ln\left|\varepsilon_{32}/\varepsilon_{21}\right| + \ln\left(\frac{r_{21}^{p_a} - s}{r_{32}^{p_a} - s}\right)\right|, \tag{11}$$

where $\varepsilon_{32} = f_3 - f_2$ and $\varepsilon_{21} = f_2 - f_1$ with f_k being the solution to the k^{th} grid, and $s = 1 \cdot \text{sign}\left(\varepsilon_{32}/\varepsilon_{21}\right)$.

The extrapolated solution $f_{\text{ext}^{21}}$ is

$$f_{\text{ext}}^{21} = \frac{\left(r_{21}^{p} f_1 - f_2\right)}{\left(r_{21}^{p} - 1\right)}, \tag{12}$$

and the approximate error e_a^{21} is

$$e_a^{21} = \left|\frac{f_1 - f_2}{f_1}\right|, \tag{13}$$

yielding and extrapolated relative error

$$e_{ext}^{21} = \left|\frac{f_{\text{ext}}^{21} - f_1}{f_{\text{ext}}^{21}}\right|, \tag{14}$$

and a grid convergence index

$$G_{CI}^{21} = \frac{1.25 e_a^{21}}{r_{21}^{p} - 1}. \tag{15}$$

The final 2D mesh, adopted following the grid convergence study, comprises 17,774 elements, with an average aspect ratio of 1.06, skewness of 0.04 and orthogonal quality of 0.99, and yielded an overall uncertainty of ±0.02%, as summarised in Table 1.

Table 1. Summary of the mesh convergence study outputs, based on [37,38].

r_{21}	r_{32}	p_a	f_{ext}^{21}	e_a^{21}	e_{ext}^{21}	G_{CI}^{21}
1.33	1.55	6.44	354.8	0.07%	0.01%	0.02%

Particular attention is given to the inlet mass flow rate $\dot{m}$. In the absence of explicit values in [25,33], it is first estimated from the mathematical model of [39], based on the experimental results of [13,40], relating the mass flow rate to the final temperature. Then, simulations are conducted for iterative values of $\dot{m}$ to identify the integer value yielding the closest results to that of [25,33]. Ultimately, $\dot{m} = 11$ g/s is retained, with the validation at the thermocouple location previously depicted in Figure 1 presented in Figure 3.

The difference in temperatures for 10 s $\leq t \leq$ 150 s is attributed to the unknowns associated with the

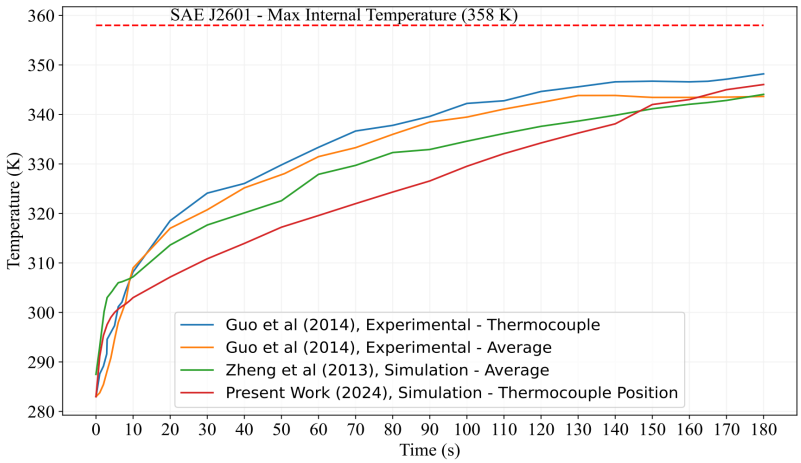

Figure 3. Comparison of the present simulation results with the experimental results of [33] and numerical results of [25] over the regulatory maximum filling time of 180 s.

mass flow rate value and any changes in rate through time in [25, 33]. However, the final temperature difference being of the order of 0.87%, and the final temperature being the primary metric associated with this study, therefore, leads to a good agreement and validation of the proposed numerical approach. This is further confirmed by the comparison of the CFD results depicted in Figure 4, where we note a difference in jet length associated with the assumptions inherent to the lack of inlet length and mass flow rate provided in [25,33].

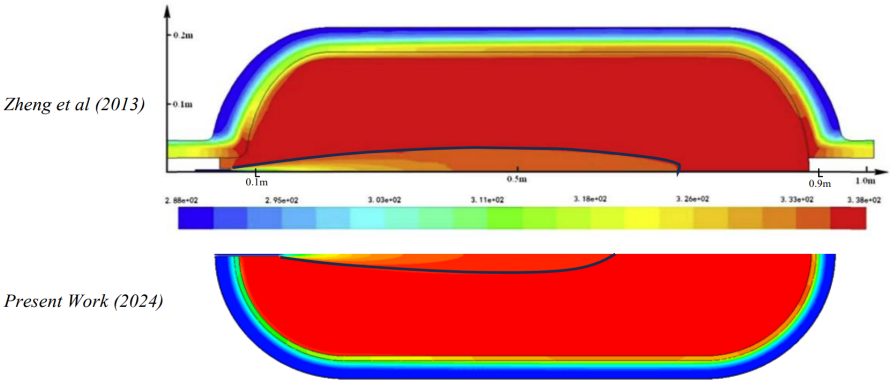

Figure 4. Comparison of the numerical results of [25] (top) with the present simulation results (bottom) at $t = 180$ s for $d = 5$ mm and $\dot{m} = 11$ g/s.

3. Results

3.1. Inlet Diameter

First, the effect of inlet diameter ranging from 5 mm to 15 mm ($0.0141 \leq d/D \leq 0.0424$) in 1 mm increments is studied at $\dot{m} = 11$ g/s. An increase in inlet diameter is associated with a monotonic increase in final temperature, as evidenced in Figure 5.

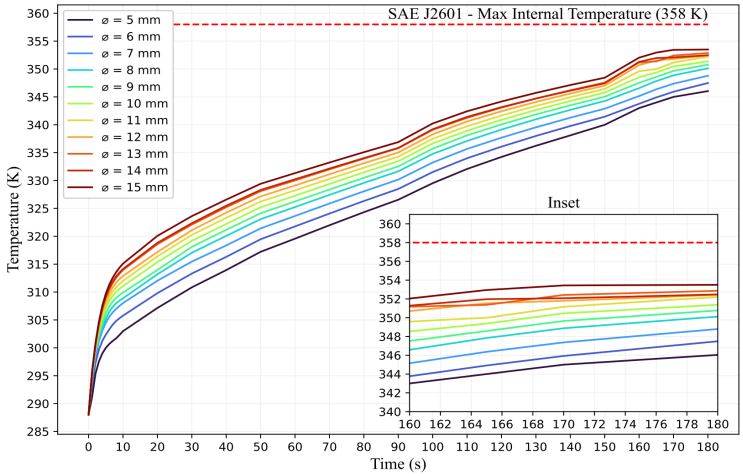

Figure 5. Effect of the inlet diameter on the temperature for 5 mm $\leq d \leq$ 15 mm at $\dot{m} = 11$ g/s.

For $\dot{m} = 11$ g/s, an increase in d/D leads to a monotonic increase in the final temperature, albeit always remaining comfortably below the SAE J2601 threshold [7]. Indeed, for the maximum tested value of $d = 15$ mm, the temperature does not exceed 353.50 K, thus ensuring the tanks investigated are safe. However, an increase in temperature can also be caused by an increase in mass flow rate [41]. Consequently, simulations were performed at $\dot{m} = 13$ g/s, with the aim being to yield non-compliant temperature to later ascertain the effect of pre-cooling.

For a mass flow rate $\dot{m} = 13$ g/s, the results in Figure 6 evidence an identical trend of monotonic increase in temperature with inlet diameter as shown for $\dot{m} = 11$ g/s. However, $d \geq 9$ mm now exceeds the $T = 358$ K

threshold, by 0.66 K for $d = 9$ mm, and by 3.94 K for $d = 15$ mm. This is significant because it allows the identification of combinations of inlet diameters and mass flow rates that would lead to a breach of automotive regulations, albeit at the expense of computational time. Consequently, in order to minimize computational effort, whether linear interpolation between mass flow rates is effective at predicting temperature is to be ascertained.

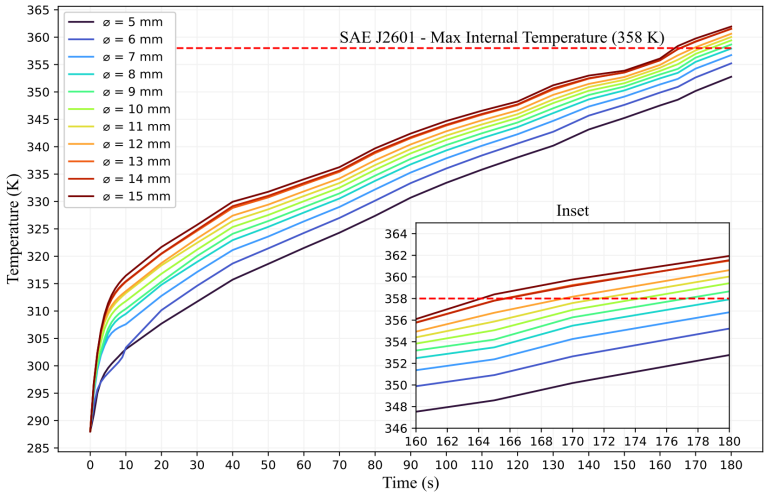

Figure 6. Effect of the inlet diameter on the temperature for 5 mm $\leq d \leq$ 15 mm at $\dot{m} = 13$ g/s.

3.2. Interpolation

A 3rd-order polynomial regression best captures the monotonic increase in temperature for increasing inlet diameter. Here, we hypothesised that a linear interpolation between $\dot{m} = 11$ g/s and $\dot{m} = 13$ g/s may be used to predict the temperature. This is investigated by comparing a linearly interpolated curve for $\dot{m} = 12$ g/s between $d = 5$ mm and $d = 15$ mm with numerical results for $\dot{m} = 12$ g/s at $d = 5$ mm, 7.77 mm, 10 mm and 15 mm, as shown in Figure 7. The values $d = 5$ mm, 10 mm and 15 mm were chosen to cover the entire parameter space under investigation, while $d = 7.77$ mm was arbitrarily chosen at the lower end of the parameter space as results at $\dot{m} = 13$ g/s indicated $d \geq 9$ mm would exceed the temperature threshold.

Thanks to the agreement between the linear interpolation and CFD data at $\dot{m} = 12$ g/s, we conclude that a

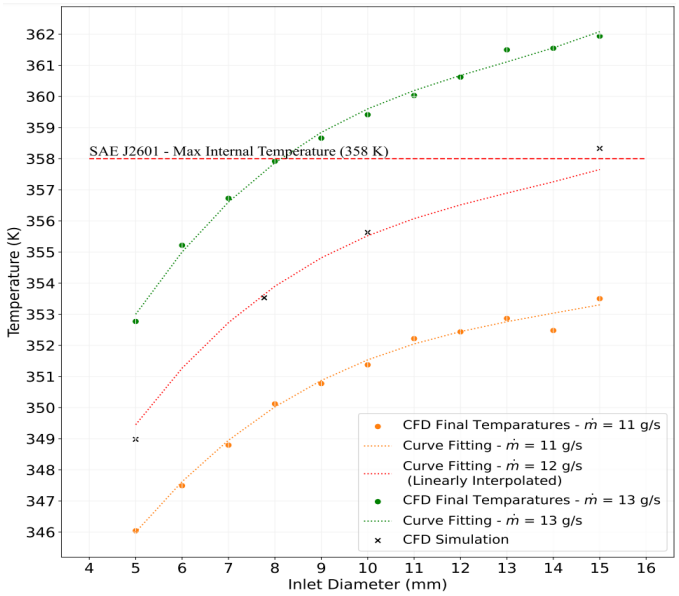

Figure 7. Variations in temperature with inlet diameter for 5 mm $\leq d \leq$ 15 mm at $\dot{m} = 11$ g/s, $\dot{m} = 12$ g/s and $\dot{m} = 13$ g/s.

linear interpolation may, therefore, be employed. This is significant as it allows to estimate the temperature at varying mass flow rates to ensure compliance with regulatory thresholds, at a much lesser computational cost. However, it is noted that the mass flow rates under consideration remain well below the SAE's maximum limit of $\dot{m} = 60$ g/s [7]. As such, for a given tank design and materials [42], pre-cooling is required [13,43]. Consequently, we next evaluate the ability of pre-cooling to reduce the tank temperature at $\dot{m} = 13$ g/s below the $T = 358$ K threshold.

3.3. Pre-Cooling

In this section, instead of the fixed inlet temperature $T = 288$ K, as defined in Section 2.2, pre-cooling is utilized. Here, pre-cooling is defined as the intentional act of reducing the temperature of the hydrogen gas to enter the inlet. To yield compliant final temperatures for the range of diameters investigated, the necessary precooling was 3 K for $d = 5$ mm, 5 K for $d = 6$ mm, 6 K for $d = 7$ mm, 7 K for $d = 8$ mm, 8 K for $d = 9$ mm, 9 K for $d = 10$ mm, 11 mm and 12 mm, and 10 K for $d = 13$ mm, 14 mm and 15 mm. Such pre-cooling by 3 K $\leq T \leq$ 10 K is shown to effectively reduce the final temperature as evidenced in Figure 8.

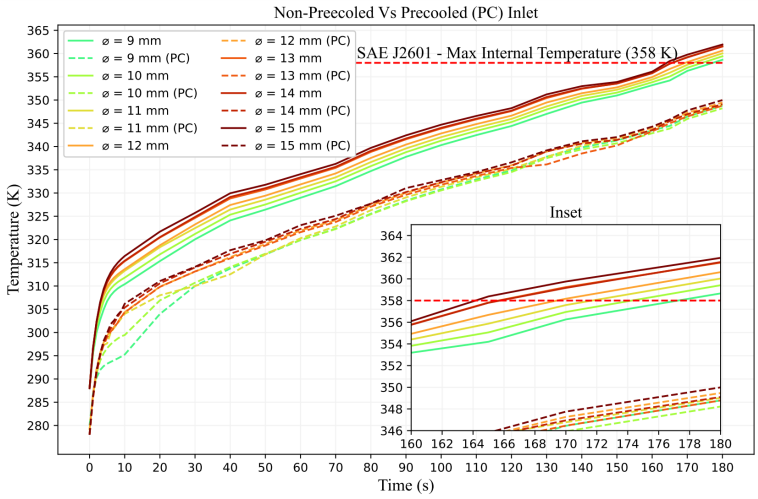

Figure 8. Effect of pre-cooling (PC) on temperature at for 5 mm $\leq d \leq$ 15 mm at $\dot{m} = 13$ g/s.

Pre-cooling the inlet is shown to be an impactful strategy towards reducing the final temperature of the tank regardless of the mass flow rate or inlet diameter. For $\dot{m} = 13$ g/s and a range of diameters 5 mm $\leq d \leq$ 15 mm, it also noted that pre-cooling results in a smaller spread in temperatures across the range of diameters investigated. Furthermore, pre-cooling does not retain the monotonic increase in temperature for increasing inlet diameter, as evidenced in Section 3.1. In contrast, a near-constant temperature can be achieved with pre-cooling, thereby alleviating the increase in temperature associated with an increase in inlet diameter. This may, therefore, prove crucial to Type III automotive tanks, which feature higher inlet-diameter-to-tank-diameter ratio than larger tanks, and thus may rely more heavily on pre-cooling to meet existing regulations.

3.4. Temperature Distribution

While pre-cooling has proven a reliable strategy, we further identify the need to investigate temperature hotspots in hydrogen tanks. Final temperature distributions, i. e., at $t = 180$ s are depicted in Figure 9, where the custom temperature scale is set such that any temperature over the SAE temperature limit [7] is clearly identified. The descending rows in Figure 9 show the temperature distribution for the increasing diameters, namely $d = 5$ mm, 10 mm and 15 mm, while columns show the two mass flow rates, $\dot{m} = 11$ g/s and $\dot{m} = 13$ g/s, respectively.

At the end of the filling process ($t = 180$ s), there are localised temperature hotspots upstream of the exit of the inlet pipe, as depicted in Figure 9c, and shown to grow for increasing diameter, see Figure 9e. This is consistent with the temperature distribution plots previously observed by [15]. These local temperature hotspots, located upstream of the inlet's exit, are the result of the separation of the boundary layer, which

causes the formation of vortices, thus leading to a higher temperature region. As the diameter increases and inlet flow velocity decreases for a constant mass flow rate, the lack of mixing between settled and newly filled hydrogen is further responsible for temperature hotspots.

We also observe an increase in the length and thickness of the jet associated with the increase in mass flow rate from $\dot{m} = 11$ g/s to $\dot{m} = 13$ g/s, leading to a higher temperature, as previously evidenced in Section 3.1. The presence of temperature hotspots, revealed through the temperature distribution across the tank, therefore showcases the importance of flow visualisation during the filling period to identify any such local temperature hotspots, ensuring temperature remains within regulatory limits.

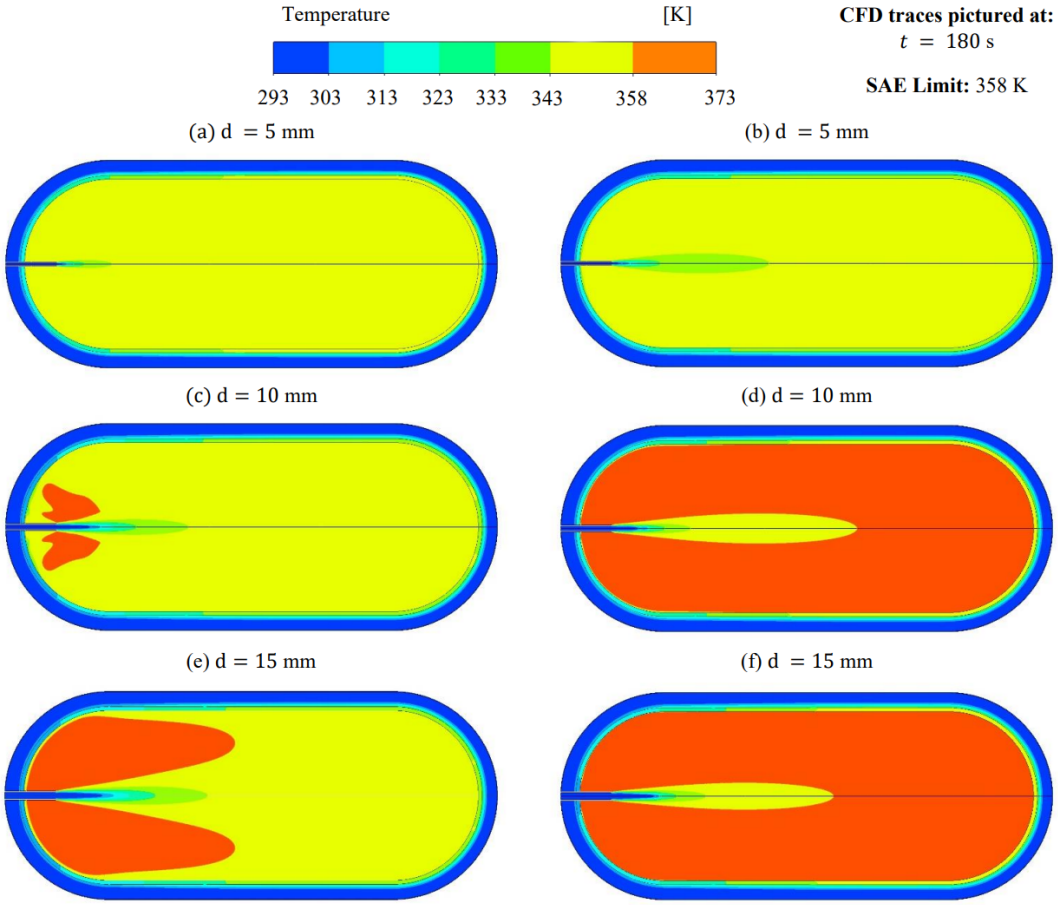

Figure 9. Temperature distribution at $t = 180$ s for $d = 5$ mm at (**a**) $\dot{m} = 11$ g/s and (**b**) $\dot{m} = 13$ g/s, $d = 10$ mm at (**c**) $\dot{m} = 11$ g/s and (**d**) $\dot{m} = 13$ g/s, $d = 15$ mm at (**e**) $\dot{m} = 11$ g/s and (**f**) $\dot{m} = 13$ g/s.

Finally, it is noted that, while the SAE regulatory threshold of T = 358 K [7] has been employed for the purpose of this study, a slightly lower threshold could be seen as appropriate in order to provide a reaction margin for internal temperature control systems to warn the user and initiate relevant safety shutdowns.

4. Conclusions

With heightened interest in Type III hydrogen gas tanks for automotive applications, characterised by a high inlet-diameter-to-tank-diameter ratio, a numerical investigation into the design parameter affecting the temperature and, therefore, regulatory compliance was undertaken using computational fluid dynamics.

Firstly, our results showed that an increase in inlet diameter results in a monotonic increase in final temperature, which is significant given the small size of Type III automotive tanks, and thus their comparatively large inlet diameter. The analysis allowed to identify combinations of inlet diameters and mass flow rates to comply with the maximum regulatory temperature.

In this work, we further evidenced that a linear interpolation between the mass flow rates tested is a

valid hypothesis, validated with additional numerical simulations. This is crucial to reduce the computational expense of ensuring regulatory compliance for land vehicles.

Moreover, we demonstrated that pre-cooling can yield a near-constant final temperature irrelevant of the inlet diameter. This is critical to alleviate the effect of large inlet diameters while remaining below the maximum temperature threshold for automotive vehicles. However, we identified the need to examine temperature distribution across the whole tank to help locate temperature hotspots. These have been shown to form upstream of the inlet and increase in size for both inlet diameter and mass flow rate.

These findings provide novel insights into the effect of inlet diameter at high inlet-diameter-to-tank-diameter and pre-cooling on the temperature of Type III hydrogen tanks for automotive applications. The results further support the design of tanks containing gaseous hydrogen to meet relevant regulations inherent to their filling and temperature. Ultimately, it is anticipated these findings may contribute to future regulatory developments, under the SAE J2601 and ISO 19881, and the wider adoption of hydrogen as a sustainable fuel.

Author Contributions: Conceptualization: M.G., J.-B.R.G.S.; formal analysis: M.G., J.-B.R.G.S.; methodology: M.G., J.-B.R.G.S.; validation: M.G., J.-B.R.G.S.; writing—original draft: M.G.; writing—review and editing: J.-B.R.G.S.; both authors have read and agreed to the published version of the manuscript.

Funding: This research received no external funding.

Institutional Review Board Statement: Not applicable.

Informed Consent Statement: Not applicable.

Data Availability: Statement: Data available on request from the authors.

Conflicts of Interest: The authors have no conflict of interest to disclose.

References

1. US Department of Energy. Alternative Fuels Data Center: Alternative Fuels and Advanced Vehicles. 2024. Available online: https://afdc.energy.gov/ fuels/(accessed on 14 June 2024).
2. European Commission. Alternative Fuels; European Commission: Brussels, Belgium, 2024. Available online: https://alternative-fuels-observatory.ec.europa.eu/general-information/ alternative-fuels(accessed on 14 June 2024).
3. Ajanovic, A.; Glatt A.; Haas R. Prospects and impediments for hydrogen fuel cell buses. *Energy* **2011,** *235*, 121340. https://doi.org/10.1016/j.energy.2021.121340.
4. Albatayneh, A.; Juaidi, A.; Jaradat, M.; Manzano-Agugliaro, F. Future of electric and hydrogen cars and trucks: An overview. *Energies* **2023**, *16*, 3230. https://doi.org/10.3390/en16073230.
5. Grube, T.; Kraus, S.; Cerniauskas, S.; Linßen, J.; Stolten, D. The market introduction of hydrogen focusing on bus refueling. *Int. J. Hydrog. Energy* **2024**, *56*, 175–187. https://doi.org/10.1016/j.ijhydene.2023.12.071.
6. Ruffio, E.; Saury, D.; Petit, D. Thermodynamic analysis of hydrogen tank filling. Effects of heat losses and filling rate optimization. *Int. J. Hydrog. Energy* **2014**, *39*, 12701–12714. https://doi.org/10.1016/j.ijhydene.2014.06.069.
7. *J2601:202005*; Fueling Protocols for Light Duty Gaseous Hydrogen Surface Vehicles, Technical Report. Society of Automotive Engineers: Warrendale, PA, USA, 2020.
8. Mori, D.; Hirose, K. Recent challenges of hydrogen storage technologies for fuel cell vehicles. *Int. J. Hydrog. Energy* **2009**, *34*, 4569–4574. https://doi.org/10.1016/j.ijhydene.2008.07.115.
9. Meduri, S.; Nandanavanam, J. Materials for hydrogen storage at room temperature–an overview. *Mater. Today Proc.* **2023**, *72*, 1–8. https://doi.org/10.1016/j.matpr.2022.05.059.
10. Galassi, M.C.; Baraldi, D.B.; Iborra, A.; Moretto, P. CFD analysis of fast filling scenarios for 70 MPa hydrogen type IV tanks. *Int. J. Hydrog. Energy* **2010**, *37*, 6886–6892. https://doi.org/10.1016/j.ijhydene.2012.01.041.
11. *ISO 19881:2018*; Gaseous Hydrogen Land Vehicle Fuel Containers. International Organization for Standardization: Geneva, Switzerland, 2018.
12. Li, Q.; Zhou, J.; Chang, Q.; Xing, W. Effects of geometry and inconstant mass flow rate on temperatures within a pressurized hydrogen cylinder during refueling. *Int. J. Hydrog. Energy* **2010**, *37*, 6043–6052. https://doi.org/10.1016/j.ijhydene.2011.12.020.
13. Cebolla, R.O.; Acosta, B.; de Miguel, N.; Moretto, P. Effect of precooled inlet gas temperature and mass flow rate on final state of charge during hydrogen vehicle refueling. *Int. J. Hydrog. Energy* **2010**, *40*, 4698–4706. https://doi.org/10.1016/j.ijhydene.2015.02.035.
14. Kim, S.C.; Lee, S.H.; Yoon, K.B. Thermal characteristics during hydrogen fueling process of type IV cylinder. *Int. J. Hydrog. Energy* **2010**, *35*, 6830–6835. https://doi.org/10.1016/j.ijhydene.2010.03.130.
15. Cui, W.; Yuan, Y.; Wang, H.; Tong, L. Numerical investigation on the influence of geometrical parameters on the temperature distribution in marine hydrogen storage tanks during filling. *Int. J. Hydrog. Energy* **2023**, *51*, 61–71. https://doi.org/10.1016/j.ijhydene.2023.10.300.

16. Liu, Y.-L.; Zhao, Y.-Z.; Zhao, L.; Li, X.; Chen, H.-G.; Zhang, L.-F.; Zhao, H.; Sheng, R.-H.; Xie, T.; Hu, D.-H.; et al. Experimental studies on temperature rise within a hydrogen cylinder during refueling. *Int. J. Hydrog. Energy* **2010**, *35*, 2627–2632. https://doi.org/10.1016/j.ijhydene.2009.04.042.
17. Heitsch, M.; Baraldi, D.; Moretto, P. Numerical investigations on the fast filling of hydrogen tanks. *Int. J. Hydrog. Energy* **2011**, *36*, 2606–2612. https://doi.org/10.1016/j.ijhydene.2010.04.134.
18. Elkhatib, R.; Louahlia, H. Metal hydride cylindrical tank for energy hydrogen storage: Experimental and computational modeling investigations. *Appl. Therm. Eng.* **2023**, *230*, 120756. https://doi. org/10.1016/j.applthermaleng.2023.120756.
19. Li, M.; Yang, Q.; Zhang, C.; Huang, S.; Zhang, M.; Zhang, G.; Zhao, L.; Jiang, S. Experimental and numerical study of the temperature evolution in hydrogen cylinder under fast-refueling process. *Int. J. Heat Mass Transf.* **2023**, *211*, 124220. https://doi.org/10.1016/j.ijheatmasstransfer.2023.124220.
20. Johnson, T.; Bozinoski, R.; Ye, J.; Sartor, G.; Zheng, J.; Yang J. Thermal model development and validation for rapid filling of high pressure hydrogen tanks. *Int. J. Hydrog. Energy* **2015**, *40*, 9803 – 9814. https://doi. org/10.1016/j.ijhydene.2015.05.157.
21. Poudel, S.; Tun, H.; Reddi, K.; Elgowainy, A. Investigation of precooling unit design options in hydrogen refueling station for heavy-duty fuel-cell electric vehicles. *Int. J. Hydrog. Energy* **2024**, *61*, 493–502. https://doi.org/10.1016/j.ijhydene.2024.02.197.
22. Tun, H.; Reddi, K.; Elgowainy, A.; Poudel, S. Thermodynamic parametric analysis of refueling heavy-duty hydrogen fuel-cell electric vehicles. Int. *J. Hydrog. Energy* **2023**, *48*, 28869 – 28881. https://doi. org/10.1016/j. ijhydene. 2023. 04.075.
23. Cardella, U.; Decker, L.; Klein, H. Roadmap to economically viable hydrogen liquefaction. *Int. J. Hydrog. Energy* **2017**, *42*, 13329–13338. https://doi.org/10.1016/j.ijhydene.2017.01.068.
24. Li, H.; Lyu, Z.; Liu, Y.; Han, M.; Li, H. The effects of infill on hydrogen tank temperature distribution during fast fill. *Int. J. Hydrog. Energy* **2021**, *46*, 10396–10410. https://doi.org/10.1016/j.ijhydene.2020.12.133.
25. Zheng, J.; Guo, J.; Yang, J.; Zhao, Y.; Zhao, L.; Pan, X.; Ma, J.; Zhang, L. Experimental and numerical study on temperature rise within a 70 MPa type III cylinder during fast refueling. *Int. J. Hydrog. Energy* **2013**, *38*, 10956–10962. https://doi.org/10.1016/j.ijhydene.2013.02.053.
26. Bilgili, M.; Yumşakdemir, R. F. Effects of real gas equations on the fast-filling process of compressed hydrogen storage tank. *Int. J. Hydrog. Energy* **2024**, *53*, 816–828. https://doi.org/10.1016/j.ijhydene.2023.12.028.
27. Tahmasebi, M.K.; Shamsoddini, R.; Abolpour B. Performances of different turbulence models for simulating shallow water sloshing in rectangular tank. *J. Mar. Sci. Appl.* **2020**, *19*, 381–387. https://doi.org/10.1007/s11804-020-00162-2.
28. Davis, P.; Rinehimer, A.; Uddin, M. A comparison of RANS-based turbulence modeling for flow over a wall-mounted square cylinder. In Proceedings of the 20th Annual Conference of the CFD Society of Canada, Canmore, AB, Canada, 9–12 May 2012; Volume 8.
29. Kannan, B.; Karthikeyan, S.; Sundararaj, S. Comparison of turbulence models in simulating axisymmetric jet flow. In *Innovative Design and Development Practices in Aerospace and Automotive Engineering*; Springer: Singapore, 2017; pp. 401–407.
30. Suryan, A.; Kim, H. D.; Setoguchi, T. Comparative study of turbulence models performance for refueling of compressed hydrogen tanks. *Int. J. Hydrog. Energy* **2013**, *38*, 9562 – 9569. https://doi. org/10.1016/j. ijhydene. 2012. 07.055.
31. Yuan, K.; Liu, Z.; Li, X. Effects of structure parameter and material property on thermal performance of on-board hydrogen storage tanks during fast refueling. *Int. J. Hydrog. Energy* **2024**, *4*, 1145–1155.
32. Yuan, K, Pan, H, Liu, Z, Andersson M. Numerical modeling for rapid charging of hydrogen gas vessel in fuel cell vehicle. *Processes* **2023**, 11, 476.
33. Guo, J.; Yang, J.; Zhao, Y.; Pan, X.; Zhang, L.; Zhao, L.; Zheng, J. Investigations on temperature variation within a type III cylinder during the hydrogen gas cycling test. *Int. J. Hydrog. Energy* **2014**, *39*, 13926–13934. https://doi.org/10.1016/j.ijhydene.2014.03.097.
34. Redlich O.; Kwong J.N. On the thermodynamics of solutions. v. an equation of state. fugacities of gaseous solutions. *Chem. Rev.* **1949**, *44*, 233–244.
35. Tan, K.; Mahajan D.; Venkatesh, T. Computational fluid dynamic modeling of methane-hydrogen mixture transportation in pipelines: Estimating energy costs. *MRS Adv.* **2022**, *7*, 388–393. https://doi.org/10.1557/s43580-022-00243-0.
36. Celik, I.; Karaismail, E.; Parsons, D. A reliable error estimation technique for CFD applications. In Proceedings of the AVT-147 Symposium on Computational Uncertainty in Military Vehicle Design, Athens, Greece, 2 December 2007.
37. Richardson, L. F. The approximate arithmetical solution by finite differences of physical problems involving differential equations, with an application to the stresses in a masonry dam. *Philos. Trans. R. Soc. London. Ser. A Contain. Pap. A Math. Phys. Character* **1911**, *210*, 307–357.
38. Celik, I. B.; Ghia, U.; Roache, P. J.; Freitas, C. J. Procedure for estimation and reporting of uncertainty due to discretization in CFD applications. *J. Fluids Eng.-Trans. ASME* **2008**, *130*. https://doi.org/10.1115/1.2960953.
39. Cheng, J.; Xiao, J.; Bénard P.; Chahine R. Estimation of final hydrogen temperatures during refueling 35 MPa and 70 tanksMPa, *Energy Procedia* **2017**, *105*, 1363–1369. https://doi.org/10.1016/j.egypro.2017.03.505.

40. Acosta, B.; Moretto, P.; De Miguel, N.; Ortiz, R.; Harskamp, F.; Bonato, C. JRC reference data from experiments of on-board hydrogen tanks fast filling. *Int. J. Hydrog. Energy* **2014**, *39*, 20531–20537. https://doi.org/10.1016/j.ijhydene.2014.03.227.
41. Li, J.-Q.; Li, J.-C.L.; Park, K.; Kwon, J.-T. Investigation on the changes of pressure and temperature in high pressure filling of hydrogen storage tank. *Case Stud. Therm. Eng.* **2022**, *37*,102143. https://doi.org/10.1016/j.csite.2022.102143.
42. Blanco-Aguilera, R.; Martinez-Agirre, M.; Berasategi, J.; Penalba, M.; Bou-Ali, M.M.; Shevtsova, V. Effect of liner thermal properties and liner pre-cooling on the thermal management of fast-filling of hydrogen tanks. *Int. J. Hydrog. Energy* **2024**, *52*, 1159–1172. https://doi.org/10.1016/j.ijhydene.2023.06.285.
43. Handa, K.; Oshima, S.; Rembutsu, T. Precooling temperature relaxation technology in hydrogen refueling for fuel-cell vehicles. *Int. J. Hydrog. Energy* **2021**, *46*, 33511–33522. https://doi.org/10.1016/j.ijhydene.2021.07.077.